electronic reprint

JOURNAL OF APPLIED CRYSTALLOGRAPHY

ISSN: 1600-5767
journals.iucr.org/j

Accurate background correction in neutron reflectometry studies of soft condensed matter films in contact with fluid reservoirs

David P. Hoogerheide, Frank Heinrich, Brian B. Maranville and Charles F. Majkrzak

J. Appl. Cryst. (2020). **53**, 15–26

IUCr Journals
CRYSTALLOGRAPHY JOURNALS ONLINE

JOURNAL OF APPLIED CRYSTALLOGRAPHY
ISSN 1600-5767

Accurate background correction in neutron reflectometry studies of soft condensed matter films in contact with fluid reservoirs

David P. Hoogerheide,[a]* Frank Heinrich,[a,b] Brian B. Maranville[a] and Charles F. Majkrzak[a]

[a]Center for Neutron Research, National Institute of Standards and Technology, Gaithersburg, MD 20899, USA, and [b]Department of Physics, Carnegie Mellon University, Pittsburgh, PA 15213, USA. *Correspondence e-mail: david.hoogerheide@nist.gov

Received 11 October 2018
Accepted 1 November 2019

Edited by G. J. McIntyre, Australian Nuclear Science and Technology Organisation, Lucas Heights, Australia

Keywords: neutron reflectometry; background subtraction; incoherent scattering; data reduction; soft condensed matter; thin films.

Neutron reflectometry (NR) is a powerful method for looking at the structures of multilayered thin films, including biomolecules on surfaces, particularly proteins at lipid interfaces. The spatial resolution of the film structure obtained through an NR experiment is limited by the maximum wavevector transfer at which the reflectivity can be measured. This maximum is in turn determined primarily by the scattering background, *e.g.* from incoherent scattering from a liquid reservoir or inelastic scattering from cell materials. Thus, reduction of scattering background is an important part of improving the spatial resolution attainable in NR measurements. Here, the background field generated by scattering from a thin liquid reservoir on a monochromatic reflectometer is measured and calculated. It is shown that background subtraction utilizing the entire background field improves data modeling and reduces experimental uncertainties associated with localized background subtraction.

1. Introduction

Specular neutron reflectometry (NR) is a powerful method for determining the compositional depth profiles of thin-film multilayered structures on length scales approaching a spatial resolution of a fraction of a nanometre. Applications are now common in many areas of science, including both hard and soft condensed matter. From a proper analysis of the neutron reflectivity of a film deposited on a flat substrate measured as a function of the glancing angle of incidence α_i, while maintaining the specular condition in which the detector defines an equal angle of reflection from the surface, the scattering length density (SLD) depth profile along the nominal surface normal can be obtained. This profile represents the average SLDs within planes parallel to the reflecting surface. Further analysis can be performed subsequently to extract the corresponding chemical compositional depth profile. The higher the required spatial resolution in the depth profile, the higher the angle up to which the reflectivity must be measured (the wavevector transfer $Q_z = 4\pi\lambda^{-1}\sin\alpha_i$, where λ is the neutron wavelength).

For a spatial resolution of 5 Å, the corresponding requisite maximum Q_z value $Q_z^{\max}$ is approximately $\pi/5$ Å $\simeq 0.6$ Å^{-1} (Schalke & Lösche, 2000; Berk & Majkrzak, 2003; Majkrzak *et al.*, 2003). For this high value of Q_z, the reflectivity for a typical 50 Å thick lipid bilayer membrane on a perfect silicon substrate is decreased by a factor of $\sim 10^7$ from unity. For soft condensed matter film structures such as lipid bilayers

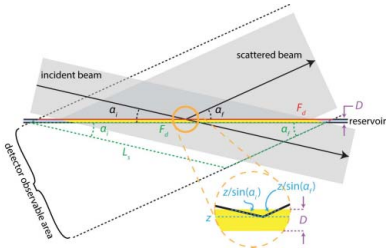

electronic reprint

deposited on relatively thick substrates and measured in contact with fluid reservoirs within flow cells, the incoherent and/or inelastic scattering background from these surrounding materials can overwhelm the signal from coherently reflected neutrons. Conversely, the fact that the coherent reflectivity is from a single interface implies that the volume of surrounding materials can be reduced to be almost arbitrarily small. While neutron reflectivity spectra with meaningful signal-to-noise ratios at a $Q_z^{\max}$ as high as 0.7 Å^{-1} have been demonstrated (Krueger *et al.*, 2001), the technical challenges have so far prevented such measurements from being routinely performed. The importance of NR for structural and applied biology (Krueger, 2001; Heinrich & Lösche, 2014; Hoogerheide *et al.*, 2017; Clifton *et al.*, 2016; Junghans *et al.*, 2015; Nylander *et al.*, 2008; Ankner *et al.*, 2013; Majkrzak *et al.*, 2006) lends some urgency to the improvement in the background from reflectometry cells and the concomitant increase in effective resolution.

Three strategies to extend $Q_z^{\max}$ are to design systems that reflect more strongly at higher Q_z, to improve background subtraction, and to reduce the background by engineering the liquid reflectometry cell. In this article, we calculate the non-isotropic background field from a typical liquid reflectometry cell. We show that the non-isotropic nature of the background field arises from self-shielding of liquid reservoirs, particularly those filled with media such as water that have large incoherent cross sections for cold neutrons. With detailed knowledge of the reflectometer geometry, the entire background field can be simply parameterized and used for improved background subtraction. The implications for the design of low-background reflectometry cells are also discussed.

2. NR of solid–liquid interfaces

2.1. Reflectometer geometry

A typical configuration of a monochromatic neutron reflectometer, such as the MAGIK vertical reflectometer (Dura *et al.*, 2006) at the NIST Center for Neutron Research (NCNR) used for all experiments in this work, is shown in Fig. 1(*a*). A monochromatic neutron beam is collimated by a pair of slits (1 and 2) such that it impinges on a sample at an average incident angle α_i. The detector is positioned at a scattering angle α_f relative to the plane of the sample (and thus an angle $\alpha_i + \alpha_f$ relative to the incident-beam direction) and an additional pair of collimating slits (3 and 4) ensure that scattered neutrons observed in the detector originate from the sample position.

The projection of the beam width onto the sample illuminates an area of the sample with 'footprint' (length in the beam direction) F_b (it is assumed that the sample dimension in the beam direction, X, is larger than F_b). For the present purposes, we will treat the case in which the pre-sample collimation is adjusted to maintain the same beam footprint at all α_i, while the post-sample collimation is adjusted to accommodate the full reflected beam width. The post-sample collimation determines the solid angle subtended by the detector, Ω_d, which is an important factor in determining the background. Here we briefly outline the dependence of Ω_d on α_i.

The beam footprint F_b depends on α_i, the openings of slits 1 and 2 (denoted S_1 and S_2, respectively), and their positions along the beam direction (L_{12} and L_{2S}, respectively) [see Fig. 1(*a*)]. The width of the beam at slit 2 is simply S_2, while the

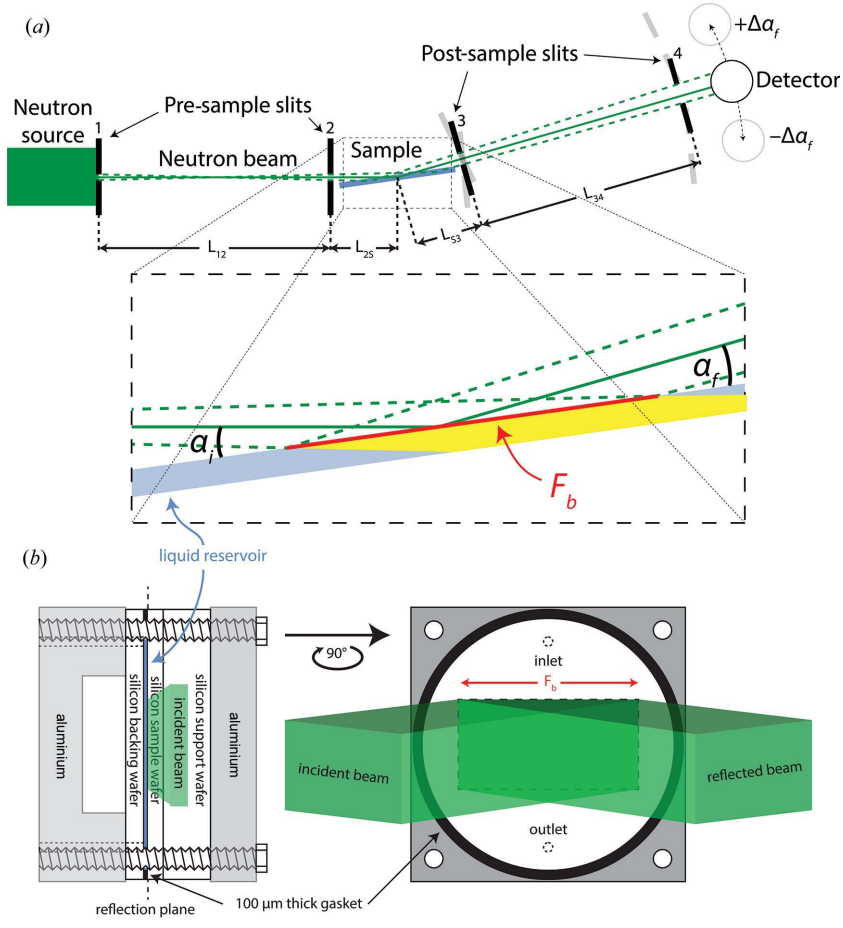

Figure 1
Monochromatic reflectometer geometry. (*a*) Collimating slits are labeled 1 through 4 in order of their position along the beam direction. Dashed lines show the maximum beam divergence. Pre-sample slit openings are chosen as a function of incident angle α_i to maintain a constant footprint F_b on the sample (expanded inset), while post-sample slit openings are chosen so as not to block any neutrons reflected from the sample when the reflection angle α_f is equal to α_i, *i.e.* the specular reflection condition. A common method of estimating the contribution of background scattering to the measured specular reflection is linear interpolation of the background field measured at larger (+) and smaller (−) detector rotations $\Delta\alpha_f$. (*b*) Schematic of NIST reflectometry cell, a stack of silicon wafers creating a reservoir of nominal thickness 100 µm. The surface of the sample wafer in contact with the liquid reservoir is the interface of interest.

electronic reprint

Table 1
Geometric configuration of the MAGIK reflectometer.

Parameter	Value
λ (Å)	5.000
X (mm)	76.2
L_{12} (mm)	1403
L_{2S} (mm)	330
L_{S3} (mm)	380
L_{34} (mm)	889
L_{4d} (mm)	406
H_d (mm)	150
$\Delta\theta_{trans}$ (°)	5.12

angular beam divergence is (for small slit openings relative to the slit separation) $\Delta\alpha = (S_1 + S_2)L_{12}^{-1}$. The width of the beam gained between slit 2 and the sample is $\Delta\alpha L_{2S}$, so the total width at the sample position is $(S_1 + S_2)L_{2S}L_{12}^{-1} + S_2$. Projecting the beam width onto the sample, which is canted at an angle α_i relative to the beam, we obtain

$$F_b \sin\alpha_i = (S_1 + S_2)L_{2S}L_{12}^{-1} + S_2. \quad (1)$$

The minimum beam divergence (and hence maximum angular resolution) is obtained if S_1 is chosen to be equal to S_2. The condition $S_1 = S_2$ is used throughout this article, though the results are readily extended to the general case in which typically $S_1 > S_2$ to increase the incident flux.

After reflecting from the sample and traveling an additional distance L_{S3} to slit 3, the beam has a width $\Delta\alpha\ (L_{2S} + L_{S3}) + S_2 = (S_1 + S_2)(L_{2S} + L_{S3})L_{12}^{-1} + S_2$. To avoid blocking any reflected neutrons, this is the minimum slit 3 opening. Typically a small offset ΔS is added to accommodate broadening of the beam from sample curvature. Then

$$S_3 = (S_1 + S_2)\big(L_{2S} + L_{S3}\big)L_{12}^{-1} + S_2 + \Delta S. \quad (2)$$

Accounting for the additional broadening between slits 3 and 4, we obtain for the slit 4 opening,

$$S_4 = (S_1 + S_2)\big(L_{2S} + L_{S3} + L_{34}\big)L_{12}^{-1} + S_2 + \Delta S. \quad (3)$$

In this work, the same ΔS is used for both slits 3 and 4. If $\Delta S > 0$, because slit 4 is further away from the sample, for scattering originating at the sample position, slit 4 provides the most collimation. The angular spread of neutrons that pass through slit 4 is

$$\Delta\alpha_4 = \tan^{-1}\left(\frac{S_4}{L_{S3} + L_{34}}\right). \quad (4)$$

In the transverse direction [out of the page in Fig. 1(*a*)], there is no post-sample collimation. The angular spread in this direction is determined by the detector height, H_d, and the sample–detector distance:

$$\Delta\theta_{trans} = \tan^{-1}\left(\frac{H_d}{L_{S3} + L_{34} + L_{4d}}\right). \quad (5)$$

The solid angle subtended by the detector is

$$\Omega_d \simeq \Delta\alpha_4\Delta\theta_{trans}. \quad (6)$$

The relevant geometric quantities for the MAGIK reflectometer are shown in Table 1.

Equation (6) assumes that the detector is always larger than S_4. For a pixelated (position-sensitive) detector, equation (6) should be replaced by the total solid angle subtended by all pixels in the region of interest.

2.2. Liquid cell for NR of solid–liquid interfaces

Fig. 1(*b*) shows the neutron-beam path through the NIST reflectometry liquid cell, which is assembled from a smooth 76.2 mm diameter silicon sample wafer, a 100 µm thick Viton gasket of outer diameter 76.2 mm and inner diameter 68 mm, and a roughened backing wafer, to create a 100 µm thick liquid reservoir filled with either pure H_2O or pure D_2O and enclosed by single-crystal silicon. For the present experiments, the sample wafer was coated with 100 Å dry thermal oxide at the NIST Center for Nanoscale Science and Technology. For the purposes of background estimation, the 'sample' comprises all cell materials exposed to the neutron beam: in this case, the sample and backing wafers and the liquid reservoir.

2.3. Measuring neutron reflectivity

The special case $\alpha_f = \alpha_i$ is the specular reflection condition, for which $Q_z = 4\pi\lambda^{-1}\sin\alpha_i$, where λ is the neutron wavelength defined by an upstream monochromator. The neutron reflectivity of a flat surface, which indicates the structure of the surface, is defined as

$$R(Q_z) = \frac{I(Q_z)}{I_0(Q_z)}, \quad (7)$$

where $I_0(Q_z)$ is the incident neutron fluence and $I(Q_z)$ is the fluence of reflected neutrons at $\alpha_i = \alpha_f$ corresponding to Q_z. The measured neutron fluence $I_{meas}(Q_z) = I(Q_z) + I_{bkg}(Q_z)$, where $I_{bkg}(Q_z)$ represents the contribution to the measured fluence from non-reflection processes such as incoherent or small-angle scattering from the volume of material surrounding the surface of interest. Thus, measuring $R(Q_z)$ entails determining $I(Q_z)$ by subtracting an estimate of $I_{bkg}(Q_z)$ (which cannot be measured directly) from $I_{meas}(Q_z)$.

For the monochromatic reflectometers at the NCNR, a typical procedure for estimating $I_{bkg}(Q_z)$ involves rotating the sample or detector twice at each Q_z value (here Q_z refers to the nominal Q_z value that would be calculated when $\alpha_f = \alpha_i$), by equal and opposite angular displacements from the specular condition, and estimating the background at the specular condition by linear interpolation (LI). We denote sample rotations by $\Delta\alpha_i$ and detector rotations by $\Delta\alpha_f$. [Note that a sample rotation for which the detector remains stationary at the original scattering angle $\alpha_i + \alpha_f$ would also involve a virtual detector rotation of $\Delta\alpha_f = -\Delta\alpha_i$.] An example of a detector rotation scheme is shown in Fig. 1(*a*). The LI background estimate is then

$$I_{bkg}^{LI}(Q_z) \simeq \frac{I^+(Q_z) + I^-(Q_z)}{2}, \quad (8)$$

electronic reprint

where $I^{+}(Q_z)$ and $I^{-}(Q_z)$ correspond to positive and negative $\Delta\alpha_i$ or $\Delta\alpha_f$. Counting times and Q_z point spacings are chosen so the statistical error of $I^{LI}_{bkg}(Q_z)$ is approximately equal to the statistical error of $I_{meas}(Q_z)$.

Fig. 2 shows the neutron reflectivity of a 100 Å thick silicon oxide film in the liquid cell. Figs. 2(*a*) and 2(*b*) show $I_{meas}(Q_z)$, $I^{+}(Q_z)$, $I^{-}(Q_z)$ and $I^{LI}(Q_z) = I_{meas}(Q_z) - I^{LI}_{bkg}(Q_z)$, all normalized to $I_0(Q_z)$, when the liquid reservoir is filled with D_2O and H_2O, respectively, and the LI method is applied to detector angular displacements $\Delta\alpha_f = \pm 0.5\alpha_i$. Fig. 2(*b*) demonstrates that the background reflectivity from the H_2O-filled reservoir is incompletely subtracted by the LI method; the 'residual' background reflectivity is $\sim 2 \times 10^{-6}$. When the reservoir is filled with D_2O, any residual background is small [Fig. 2(*a*)]. The origin of the residual background is clear from the insets in Fig. 2, which show the measured neutron fluence $I_{meas}(Q_z)$ when $\Delta\alpha_f$ is scanned from $-0.75\alpha_i$ to $0.75\alpha_i$ at a nominal Q_z value of 0.15 Å^{-1}. The background from the D_2O-filled reservoir does not vary systematically between the measurement values (vertical dashed lines), while the background from the H_2O-filled reservoir has significant negative curvature, leading to an underestimate of the background at the specular condition by the LI method.

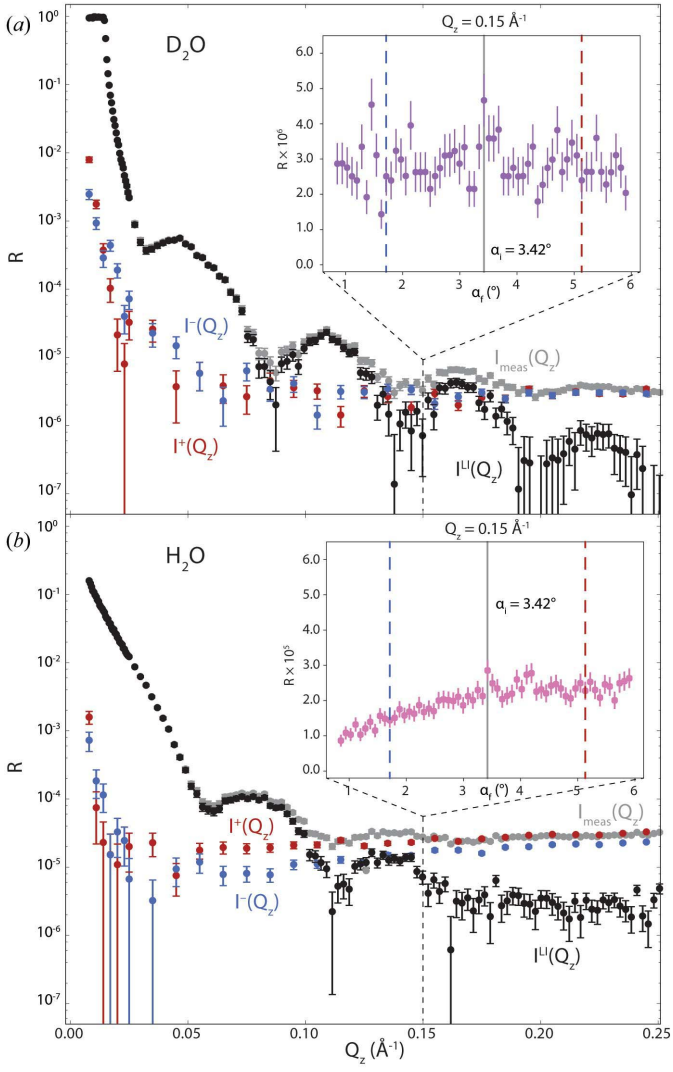

Figure 2
Neutron reflectivity of a 100 Å silicon dioxide film at a silicon–liquid interface showing the results of an LI background estimation when the liquid is pure D_2O (*a*) or H_2O (*b*). $I_{meas}(Q_z)$, $I^{+}(Q_z)$ and $I^{-}(Q_z)$ denote the measured neutron fluence at the specular condition, with positive detector angular displacement and with negative detector angular displacement, respectively. The result of a point-wise LI subtraction is denoted by $I^{LI}(Q_z)$. All quantities are normalized to the incident-beam intensity $I_0(Q_z)$. (Insets) Detector angle (transverse) scans at a nominal $Q_z = 0.15$ Å^{-1}. Vertical dashed lines denote the position of background-field estimation, while the solid line represents the specular condition. Error bars represent 68% confidence intervals based on Poisson counting statistics.

Thus, a background-subtraction method that accounts for the curvature of the background is required. Polynomial fitting to transverse scans is impractical because of the large increase in the number of background data points required at each Q_z value. The use of a position-sensitive detector would allow the transverse measurement to be performed simultaneously with the measurement of the specular reflection; however, this requires either installation of a specially designed radial collimator or reduction of the post-sample collimation. Reduction of the post-sample collimation increases the field of view of the detector and risks the introduction of additional sources of background. Instead, a prediction of the background field that is simply parameterized and can be measured in a relatively short measurement time is required.

3. Theory

We define the background field as the neutron intensity from scattering from a liquid cell as measured by a reflectometer in an arbitrary configuration comprising α_i, α_f, the slit openings [equations (1)–(3)] and the detector solid angle [equation (6)]. To derive an expression for the background field, the background scattering is supposed to arise entirely from scattering from the sample cell, which comprises structural materials that define a thin flat liquid reservoir. We assume that neutrons scatter only once or at most twice through the material (the strongly scattering case is revisited at the end of this section). This allows us to write the total probability $P(\alpha_i, \alpha_f)$ that an incident neutron at an angle of incidence of α_i is scattered into a detector at a scattered angle of α_f as the product of the probability that a neutron scatters in a volume of the material viewed by the detector, $P_{sc}(\alpha_i, \alpha_f)$, and the probability that a neutron is scattered into the detector solid angle Ω_d and arrives there without scattering again, $P_d(\alpha_i, \alpha_f)$:

$$P(\alpha_i, \alpha_f) = P_{sc}(\alpha_i, \alpha_f)\, P_d(\alpha_i, \alpha_f). \quad (9)$$

Given an incident fluence I_0 impinging on the sample, the observed background fluence I is simply $I = PI_0$, assuming $R \ll 1$.

Here we separately consider the two cases of scattering from the reservoir and scattering from the structural materials. The geometry used to calculate the background field is shown in Fig. 3. To characterize the strength of the scattering, we introduce the attenuation coefficient (inverse attenuation length) ε for scattering from the reservoir and ε_s for scattering

electronic reprint

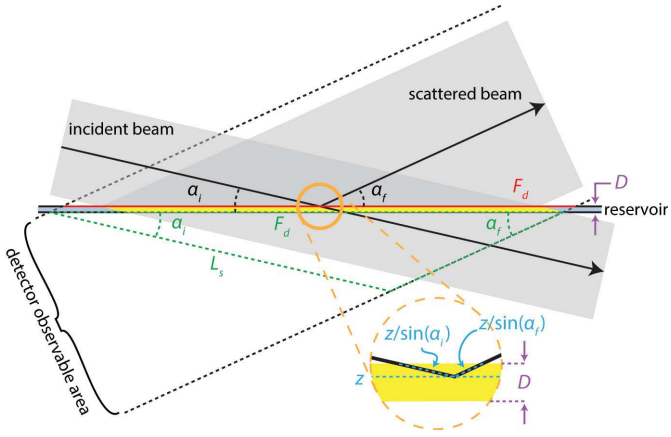

Figure 3
Geometry used for calculating the theoretical background field. The inset shows the scattering depth (and integration variable) z. The reservoir thickness is D.

from the structural materials of the cell, in this case silicon. All scattering is assumed to be isotropic. The attenuation coefficient is related to the incoherent cross section $\sigma_{\rm inc}$ and number density n of the material by

$$\varepsilon = \sigma_{\rm inc} n, \tag{10}$$

and can be calculated using tabulated values (Sears, 1992).

3.1. Reservoir scattering

Consider a neutron traveling through a reservoir at an angle $\alpha_{\rm i}$. We denote the probability that the neutron arrives at a depth z (see Fig. 3) by $P(z, \alpha_{\rm i})$. The probability that the neutron scatters in any slab of infinitesimal thickness dz is, by definition of the attenuation coefficient, $P_{\rm slab}(\alpha_{\rm i}) = \varepsilon\, {\rm d}z/\sin\alpha_{\rm i}$. Thus, the infinitesimal reduction in $P(z, \alpha_{\rm i})$ across a slab of thickness dz is the joint probability that the neutron arrives at a depth z, $P(z, \alpha_{\rm i})$, and that it scatters in a thickness dz (depth-independent probability). Thus,

$${\rm d}P(z, \alpha_{\rm i}) = -P_{\rm slab}(\alpha_{\rm i})\, P(z, \alpha_{\rm i}) = -\frac{\varepsilon\, {\rm d}z}{\sin\alpha_{\rm i}} P(z, \alpha_{\rm i}). \tag{11}$$

This is the governing equation for $P(z, \alpha_{\rm i})$ and, with the boundary condition $P(0, \alpha_{\rm i}) = 1$, can be easily solved to obtain

$$P(z, \alpha_{\rm i}) = \exp\left(-\frac{\varepsilon z}{\sin\alpha_{\rm i}}\right). \tag{12}$$

The joint probability that a neutron incident on the reservoir both arrives at depth z and scatters in a slab of thickness dz at that depth is $P_{\rm sc}(z, \alpha_{\rm i}) = P_{\rm slab}(\alpha_{\rm i}) P(z, \alpha_{\rm i})$ or

$$P_{\rm sc}(z, \alpha_{\rm i}) = \frac{\varepsilon\, {\rm d}z}{\sin\alpha_{\rm i}} \exp\left(-\frac{\varepsilon z}{\sin\alpha_{\rm i}}\right). \tag{13}$$

[This expression also follows directly from equation (11).] If a neutron scatters isotropically at a depth z, its probability of scattering in the direction of the detector is $\Omega_{\rm d}/4\pi$. The neutron must then travel a distance $z/\sin\alpha_{\rm f}$ through the reservoir to be observed by the detector. Such neutrons are similarly exponentially attenuated over this path length, so the probability of such a neutron being observed by the detector is

$$P_{\rm d}(z, \alpha_{\rm f}) = \frac{\Omega_{\rm d}}{4\pi} \exp\left(-\frac{\varepsilon z}{\sin\alpha_{\rm f}}\right). \tag{14}$$

This expression is analogous to equation (12), just from the point of view of a source of neutrons located at depth z. Here the reservoir is assumed to be sufficiently thin that the spread of the beam through the reservoir can be neglected. The net fluence into the detector from a reservoir of thickness D is then the total contribution from all possible scattering depths z:

$$I_{\rm res}(\alpha_{\rm i}, \alpha_{\rm f}) = I_0 \int_{z=0}^{D} P_{\rm d}(z, \alpha_{\rm f}) P_{\rm sc}(z, \alpha_{\rm i}) = I_0 \frac{\Omega_{\rm d}}{4\pi} \frac{\varepsilon}{\sin\alpha_{\rm i}} \times \int_0^D \exp\left[-\varepsilon z\left(\frac{1}{\sin\alpha_{\rm i}} + \frac{1}{\sin\alpha_{\rm f}}\right)\right] {\rm d}z \tag{15}$$

and

$$\frac{I_{\rm res}(\alpha_{\rm i}, \alpha_{\rm f})}{I_0} = \frac{\Omega_{\rm d}}{4\pi} \frac{\left(1 - \exp\left\{-\varepsilon D\left[(1/\sin\alpha_{\rm i}) + (1/\sin\alpha_{\rm f})\right]\right\}\right)}{1 + \sin\alpha_{\rm i}/\sin\alpha_{\rm f}}. \tag{16}$$

In the limit of very weak scattering, or very thin reservoirs, $\varepsilon D \ll 1$,

$$\frac{I_{\rm res}(\alpha_{\rm i}, \alpha_{\rm f})}{I_0} = \frac{\Omega_{\rm d}}{4\pi} \frac{\varepsilon D}{\sin\alpha_{\rm i}}. \tag{17}$$

In this limit, neutrons scattered in the direction of the detector are not attenuated at all; thus, the dependence on $\alpha_{\rm f}$ disappears and only a linear dependence on the path length of the incident beam through the reservoir, $D/\sin\alpha_{\rm i}$, remains.

In the limit of strong scattering, the exponential term (and the dependences on both the attenuation coefficient and the reservoir thickness) vanishes and

$$\frac{I_{\rm res}(\alpha_{\rm i}, \alpha_{\rm f})}{I_0} = \frac{\Omega_{\rm d}}{4\pi} \frac{1}{1 + \sin\alpha_{\rm i}/\sin\alpha_{\rm f}}. \tag{18}$$

The entire beam scatters into background. For the MAGIK reflectometer using collimation corresponding to a specular $Q_z = 4\pi\lambda^{-1}\sin\alpha_{\rm i} = 0.25$ Å^{-1} and a sample footprint of 50 mm, the background level would be $I_{\rm res}/I_0 = 6.7 \times 10^{-5}$. Note that this limit violates the single-scattering assumption used in calculating $P_{\rm d}$, so equation (18) is not expected to be quantitative. In the limit of a thick strongly scattering reservoir ($\varepsilon D/\sin\alpha_{\rm i} > 1$), or if the beam passes through strong incoherently scattering materials after passing through the reservoir such that the beam transmission through the cell is negligible, the entire beam [not half, as predicted by equation (18)] will be scattered, in general anisotropically, back from the sample into the incident half-space. Treatment of this case requires numerical or approximation solutions (Chandrasekhar, 1960; Hottel & Sarofim, 1967). Using $\sin\alpha_{\rm i} \simeq 0.1$, εD is limited to 0.1 for the current treatment to be accurate. This corresponds to a 180 µm thick reservoir for H_2O-based solutions and a 7.4 mm

electronic reprint

thick reservoir for D_2O-based solutions, using attenuation coefficients of 5.435 and 0.1357 cm^{-1}, respectively, calculated from tabulated values (Sears, 1992).

3.2. Scattering from cell materials

We assume that the beam travels through a homogeneous material of attenuation coefficient ε_s, and that the product of the attenuation coefficient and the total beam path through the cell is much smaller than 1. In this limit of very weak scattering, the beam attenuation is small, allowing us to forgo the integration over the scattering depth. Let L_s be the path length of the incident beam across the volume of the cell that can scatter into (*i.e.* is viewed by) the detector (Fig. 3). For very tight post-sample collimation, as shown in Fig. 3, this length is most conveniently expressed in terms of the footprint in the plane of the reservoir that would be illuminated if the beam came from the detector rather than from the source, F_d:

$$L_s = \frac{F_d \sin\alpha_f}{\sin(\alpha_i + \alpha_f)}. \tag{19}$$

For looser post-sample collimation, in which the entire path of the incident beam through a cell of dimension X in the beam direction is observed by the detector, the expression is simpler:

$$L_s = \frac{X}{\cos\alpha_i}. \tag{20}$$

In general, equation (20) should be used when $X < F_d$.

We must distinguish between neutrons that scatter in the cell materials on the two sides of the reservoir. Each has an average path length $L_s/2$, but the beam is attenuated by $\exp(-\varepsilon D/\sin\alpha_i)$ after passing through the reservoir. Thus, the probability of scattering before reaching the reservoir is

$$P_{sc,before}(\alpha_i) = \frac{\varepsilon_s L_s}{2}, \tag{21}$$

while the probability of scattering after passing through the reservoir is

$$P_{sc,after}(\alpha_i) = \frac{\varepsilon_s L_s}{2}\exp\left(-\frac{\varepsilon D}{\sin\alpha_i}\right). \tag{22}$$

The probability that a neutron is scattered into the detector, P_d, also depends on whether the neutron was scattered before reaching or after passing through the reservoir. In the former case, $P_{d,before}(\alpha_f) = \Omega_d/4\pi$; in the latter, the scattered neutron is further attenuated, such that $P_{d,after}(\alpha_f) = (\Omega_d/4\pi)\exp(-\varepsilon D/\sin\alpha_f)$.

In total,

$$\frac{I_s(\alpha_i,\alpha_f)}{I_0} = P_{sc,before}\,P_{d,before} + P_{sc,after}\,P_{d,after} \tag{23}$$

and

$$\frac{I_s(\alpha_i,\alpha_f)}{I_0} = \varepsilon_s L_s\left\{\frac{1}{2} + \frac{1}{2}\exp\left[-\varepsilon D\left(\frac{1}{\sin\alpha_i} + \frac{1}{\sin\alpha_f}\right)\right]\right\}\frac{\Omega_d}{4\pi}. \tag{24}$$

Equation (24) does not apply unless $\varepsilon_s L_s \ll 1$. This stipulation is violated in common NR cell designs in which the backing material is not single-crystal silicon but other materials with a larger incoherent attenuation coefficient, such as steel or hydrogen-containing fluoropolymers. This case is analogous to the limit of infinite thickness of scattering by the reservoir discussed at the end of the previous section. In this case a large fraction of the incident beam is scattered into background; after multiple scattering events, all the neutrons eventually emerge from the surface of the reservoir facing the incident beam and may find their way to the detector. The estimate of a possibly anisotropic background at the 10^{-5} level also applies here.

3.3. Other sources

Other environmental or systematic sources of background, such as stray high-energy radiation or dark current in the detector system, contribute a constant neutron counting rate ν_{other}, so that the apparent intensity depends only on the counting time Δt:

$$\frac{I_{other}}{I_0} = \frac{\nu_{other}\Delta t}{I_0}. \tag{25}$$

3.4. Total background field

The total background reflectivity is

$$\frac{I_{bkg}(\alpha_i,\alpha_f)}{I_0} = \frac{I_{res}(\alpha_i,\alpha_f)}{I_0} + \frac{I_s(\alpha_i,\alpha_f)}{I_0} + \frac{I_{other}}{I_0}. \tag{26}$$

3.5. Implementation in *reductus*

The background-field subtraction technique, comprising equations (16) and (24), has been implemented in the *reductus* software package routinely used at the NCNR for data reduction (Maranville *et al.*, 2018). The workflow consists of fitting of the background-field parameter εD to intensity-normalized background data, then subtracting the calculated background field from the intensity-normalized specular reflection data.

4. Experiments

To test the theoretical predictions, we performed transverse (α_f) scans, such as those shown in the insets to Fig. 2, for multiple Q_z values. Table 2 shows the slit openings and derived divergences for select values of α_i in the experiments.

The data are shown in Fig. 4 normalized to the incident-beam intensity, so that the levels correspond to the background-reflectivity level. Both data and incident-intensity scans are normalized by an inline monitor rate to account for fluctuations in beam intensity. The sample angle α_i is shown by the vertical dashed line.

To extract the contribution of the silicon cell materials, the 19 mm thick single-crystal Si(100) wafer used as the silicon

electronic reprint

Table 2
Collimation settings.

ΔS = 1.22 mm and X = 76.2 mm. F_d is shown for $\alpha_f = \alpha_i$.

Q_z (Å^{-1})	α_i (°)	$S_1 = S_2$ (mm)	S_3 (mm)	S_4 (mm)	F_b (mm)	F_d (mm)	$\Delta\alpha_4$ (°)	Ω_d $\times 10^3$
0.1	2.280	1.352	3.846	6.042	50.0	203	0.273	0.426
0.15	3.422	2.029	5.159	8.453	50.0	184	0.382	0.596
0.2	4.564	2.707	6.472	10.864	50.0	174	0.491	0.766
0.25	5.709	3.382	7.785	13.277	50.0	169	0.599	0.934

support wafer [see Fig. 1(*b*)] was mounted in an evacuated vacuum chamber. The wafer was rotated around its center axis so the beam was misaligned by about 20° from the [220] crystal direction. The beam was then aligned to pass through the center of the wafer. Data were collected with the same protocols used to study the liquid cell. Finally, the intrinsic background limit due to 'dark counts' in the absence of any materials in the beam was measured after removing the silicon from the vacuum chamber.

To obtain the solid lines in Fig. 4, equation (26) was optimized to the experimentally determined background fields using a Levenberg–Marquardt optimization algorithm. Because εD always occurs as a product in equations (16) and (24) and the exact thickness of the reservoir is not known, the products $\varepsilon_{H_2O}D$ and $\varepsilon_{D_2O}D$ were chosen as free parameters. Equation (20) was used to estimate L_s. Parameter uncertainties were estimated from the covariance matrix. The four free parameters and their optimized values and uncertainties are shown in Table 3, where they are compared to their nominal values based on equation (10), tabulated values of the incoherent cross sections of H, D, O and Si (Sears, 1992), and the nominal 0.01 cm thickness of the reservoir. The normalized χ^2 value was 1.12.

Table 3
Determination of scattering properties by optimizing data to the background-field model.

Parameter	Value (68% confidence intervals)	Nominal value
$\varepsilon_{H_2O}D$	5.417 (73) $\times 10^{-2}$	5.435 $\times 10^{-2}$
$\varepsilon_{D_2O}D$	0.2354 (43) $\times 10^{-2}$	0.1357 $\times 10^{-2}$
$\varepsilon_{s,Si}$ (cm^{-1})	1.109 (21) $\times 10^{-3}$	1.998 $\times 10^{-4}$
ν_{other} (min^{-1})	3.587 (83)	—

The agreement between the nominal attenuation coefficient of H_2O and the value obtained from the optimization is within statistical error. The attenuation coefficient in D_2O is larger than its nominal value by about 70%; this suggests that a small amount of H_2O is present in the D_2O. The attenuation coefficient of a fraction x of H_2O in a binary mixture with D_2O is related to the nominal attenuation coefficients of H_2O and D_2O by $\varepsilon = x\varepsilon_{H_2O} + (1 - x)\varepsilon_{D_2O}$. This calculation yields $x \simeq 1.9\%$, which is reasonable given the hygroscopic nature of D_2O and the possibility of incomplete solvent exchange in the flow cell.

Interestingly, the attenuation coefficient of silicon is nearly an order of magnitude larger than that expected for incoherent scattering from silicon. This suggests that other processes contribute to the background field. A recent measurement of inelastic scattering of 8 Å neutrons incident from the [220] direction of single-crystal silicon (Barker & Mildner, 2015) yields $\varepsilon_{s,Si} \simeq 6.3 \times 10^{-3}$cm^{-1}. Because inelastic scattering is not, in general, isotropic, care must be taken for cell designs in which inelastic scattering contributes a significant fraction to the background field. However, for the purposes of the present calculation and practical reflectometry cell design, the isotropic assumption appears to be sufficient. Importantly, the product $\varepsilon_{s,Si}L_s \simeq 8.5 \times 10^{-3} \ll 1$, thereby justifying the assumption of weak scattering from the silicon used to derive equation (24).

The value of ν_{other} is found to be about 3.6 counts per minute for the MAGIK reflectometer. In apparent

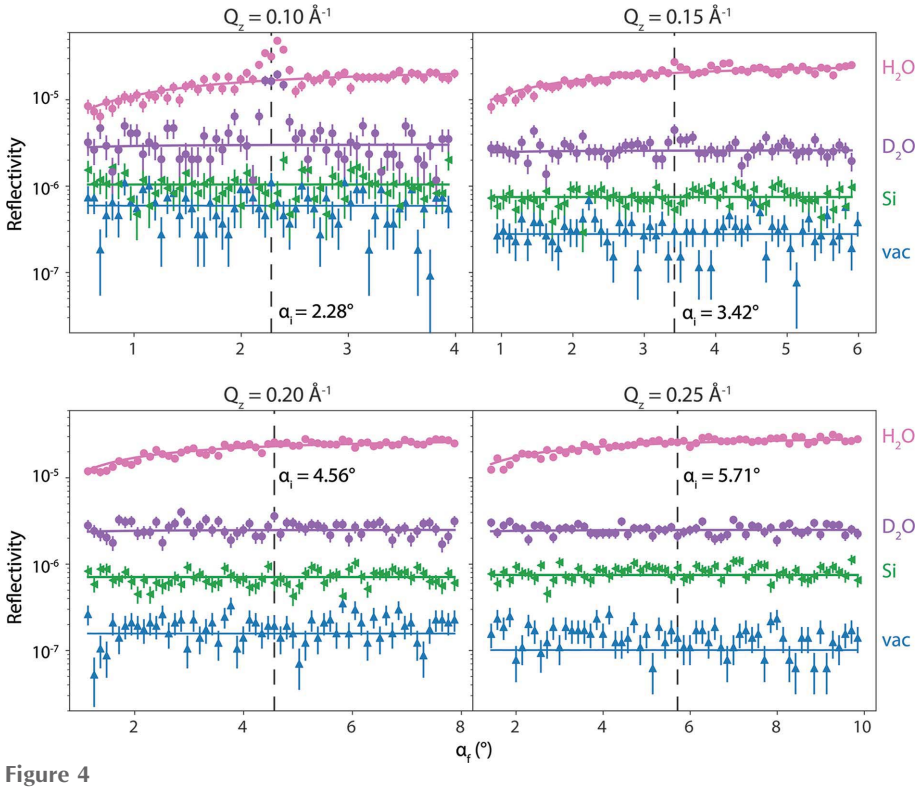

Figure 4
Background field of a liquid reflectometry cell at various incident-beam angles. The liquid reservoir was nominally 100 µm thick and filled with pure H_2O (pink circles) or D_2O (purple diamonds). Also shown are the background fields from an Si single crystal in vacuum (green left-pointing triangles) and from the vacuum (blue upward-pointing triangles) after removing the Si. Solid lines show the result of fitting the theoretical prediction of the background field to the experimental data. Error bars represent 68% confidence intervals based on Poisson counting statistics.

electronic reprint

reflectivity, this is an order of magnitude smaller than the scattering from silicon at Q_z values above 0.15, where scattering background becomes significant, and is thus of little practical importance at these values.

5. Implications for background estimation and subtraction

As shown in both Fig. 2 and Fig. 4, the background field from the H_2O-filled reservoir has a nonlinear dependence on α_f, while the D_2O and Si background fields are much flatter. This is because of the 'self-shielding' effect of the H_2O reservoir at small detector angles, in which the path length of neutrons through the reservoir is significant relative to the attenuation length. Thus, neutrons that are initially scattered in the direction of the detector have a significant probability of scattering again before exiting the sample film. For the D_2O-filled reservoirs, this effect is less pronounced because the incoherent attenuation coefficient is much smaller.

5.1. Performance of LI background estimation methods

LI-based procedures for estimating the background under a specular reflection signal have already been introduced and, in the case of detector angle rotations, shown to leave significant residual background, particularly for H_2O-filled reservoirs. To account for this residual background, an additional constant (*i.e.* Q_z-independent) background (CB) is often included in analysis models or used in place of LI subtraction. Here we consider two LI methods: (1) rotating the detector such that $\Delta\alpha_f/\alpha_f$ is constant throughout a Q_z scan and (2) rotating the sample so that $\Delta\alpha_i/\alpha_i$ is constant throughout a Q_z scan.

The solid curves in Fig. 5(*a*) show the residual background, *i.e.* the fraction of the calculated background field unaccounted for by the LI method, for H_2O and D_2O reservoirs, using detector rotation angles $\Delta\alpha_f = \alpha_i/2$ and holding $\Delta\alpha_f/\alpha_f$ constant with Q_z. The calculation follows from equation (26) with $I_{other} = 0$:

$$1 - \frac{I_{bkg}^{LI}(\alpha_i, \alpha_f = \alpha_i)}{I_{bkg}(\alpha_i, \alpha_f = \alpha_i)} = 1 - \tfrac{1}{2}\left[I_{bkg}(\alpha_i, \alpha_i + 0.5\alpha_i) + I_{bkg}(\alpha_i, \alpha_i - 0.5\alpha_i)\right] \Big/ I_{bkg}(\alpha_i, \alpha_i). \quad (27)$$

This 'fractional residual background' is about 0.2% for D_2O-filled reservoirs at $Q_z = 0.25\text{Å}^{-1}$, which typically have a measured background of 1.5×10^{-6}, representing a residual background of 2.9×10^{-9}. The Fresnel reflectivity at $Q_z = 0.25\text{Å}^{-1}$ from the Si/D_2O interface is about 7.2×10^{-7}, so this underestimate is more than two orders of magnitude smaller than the signal and only marginally degrades the signal-to-noise ratio. On the other hand, for H_2O-filled reservoirs, both the background itself (2.3×10^{-5}) and the fractional residual background (~5.5%) are significantly larger, representing an excess background of 1.3×10^{-6}. This cannot be fully accounted for by a CB correction because the residual background varies by nearly 40% of its value from $Q_z = 0.1$ to 0.25 Å^{-1}, and by 80% out to the large Q values that NR experiments aspire to. The Fresnel reflectivity from the Si/H_2O interface is only 2.4×10^{-7} at $Q_z = 0.25$ Å^{-1}, so the residual background represents a significant degradation of signal-to-noise ratio. Subtraction of the background field using equation (26) would significantly increase the Q_z range over which NR data from H_2O-filled reservoirs provide useful information and hence the resolution of the measurement. This effect is quantified in Fig. 5(*b*), which shows the ratio of the silicon–liquid Fresnel reflectivity to the residual background from the LI method. This ratio should be interpreted as an upper limit on the signal-to-noise ratio achievable using the LI method. For H_2O, the ratio drops below unity at $Q_z \simeq 0.15$ Å^{-1}, similar to the Q_z value at which the residual

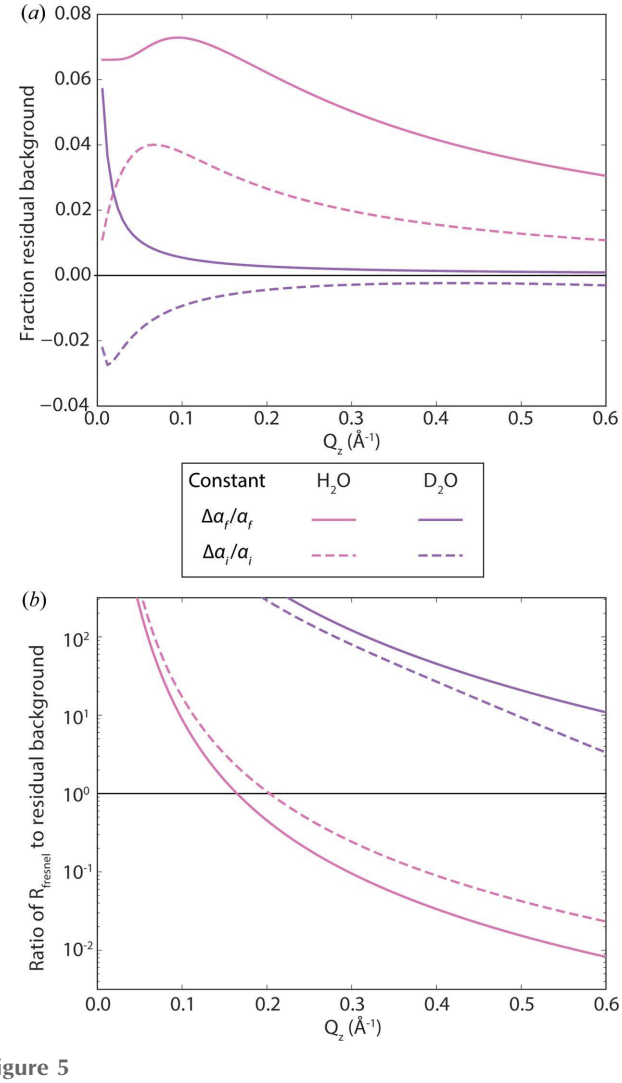

Figure 5
Limitations of two different forms of the LI methods of background subtraction for reservoirs filled with D_2O and H_2O: (1) moving the detector by a fixed fraction of the detector angle (constant $\Delta\alpha_f/\alpha_f = 0.5$) and (2) rocking the sample by a fixed fraction of the sample angle (constant $\Delta\alpha_i/\alpha_i = 0.25$), while maintaining a constant beam footprint on the sample. (*a*) Fraction of background field unaccounted for by the LI method. Negative values represent overestimation of the background. (*b*) Ratio of the Fresnel reflectivity of the silicon–liquid interface to the residual background after LI subtraction. This ratio represents the upper limit of the signal-to-background ratio achievable with LI.

electronic reprint

background dominates the specular reflectivity in Fig. 2(*b*). For D_2O, the residual background is not significant until $Q_z > 0.6$ Å^{-1}.

The dashed curves in Fig. 5 show the effect of the second LI technique (constant $\Delta\alpha_i/\alpha_i$), in which the sample angle α_i is rotated to 0.75 and 1.25 times its value at the specular condition (while not moving the detector so that α_f is 1.25 and 0.75 times its value at the specular condition, respectively). Importantly, the pre-sample collimation is adjusted to maintain a constant F_b when rotating the sample. The expression is

$$1 - \frac{I^{\rm LI}_{\rm bkg}(\alpha_i, \alpha_f = \alpha_i)}{I_{\rm bkg}(\alpha_i, \alpha_f = \alpha_i)} = 1 - \tfrac{1}{2}\big[I_{\rm bkg}(\alpha_i - 0.25\alpha_i, \alpha_i + 0.25\alpha_i) + I_{\rm bkg}(\alpha_i + 0.25\alpha_i, \alpha_i - 0.25\alpha_i)\big] \big/ I_{\rm bkg}(\alpha_i, \alpha_i). \quad (28)$$

This procedure slightly outperforms the detector rotation scheme; however, in both cases the residual background varies with Q_z so a CB correction cannot be readily applied.

5.2. Effects of background-field subtraction on model fitting

To test the effects of different background-subtraction techniques on model fitting, the reflectivity from the 100 Å thermal oxide film was reduced two ways using the *reductus* software implementation: (1) using LI background estimation from detector-rotated background scans [$I^{\rm LI}(Q_z)$ from Fig. 2] and (2) using background-field (BF) subtraction. For the latter, the product εD was fitted to equation (26), using $\varepsilon_{s,Si} = 1.109 \times 10^{-3}$ cm^{-1}and $I_{other} = 0$, independently for both the D_2O and H_2O background data shown in Fig. 2 for $Q_z > 0.05$ Å^{-1}. The error in the fit parameter was estimated from the covariance. The results were $\varepsilon_{D_2O}D = (0.2737 \pm 0.0073) \times 10^{-2}$ and $\varepsilon_{H_2O}D = (5.358 \pm 0.082) \times 10^{-2}$; these were used to calculate and subtract the background field at the specular condition, again using equation (26).

Data reduced using LI or BF subtraction were each subsequently fitted to two slab models (Ankner & Majkrzak, 1992) of the oxide layer which differed only in that one included a CB correction. The basic model included the following parameters: the thermal silicon oxide thickness, the oxide SLD, the substrate roughness (applied to both the Si/oxide and oxide/solvent interfaces), the solvent SLDs and an intensity correction that scales the entire reflectivity curve. The model including the CB correction had one additional parameter for each solvent included: the magnitude of the constant (Q_z-independent) background. Optimizations were performed using *Refl1D* (Kienzle *et al.*, 2016) on the Bridges (Nystrom *et al.*, 2015; Towns *et al.*, 2014) high-performance computing system using the DREAM Markov chain Monte Carlo algorithm. (Vrugt *et al.*, 2009). Confidence intervals on parameters and model predictions are calculated from about 360 000 DREAM samples after the optimizer has reached steady state. Modeling results are shown in Table 4 and the Fresnel-normalized reflectivities are shown in Fig. 6.

The modeling results in Table 4 demonstrate the immediate advantage of the BF subtraction method. For joint optimizations using both D_2O and H_2O data, the BF subtraction method is essentially equivalent to the LI + CB methods, as shown by the similar χ^2 values, even in the absence of background parameters in the model. When included in the BF + CB model, the background parameters are consistent with zero, demonstrating conclusively that they are not required when using BF subtraction. By contrast, the background parameters are necessary to avoid inflated χ^2 values when using LI subtraction.

5.3. Effect on counting time

An important limitation of LI subtraction is that significant time is spent measuring the background because the noise of the measurement depends on obtaining sufficient counting

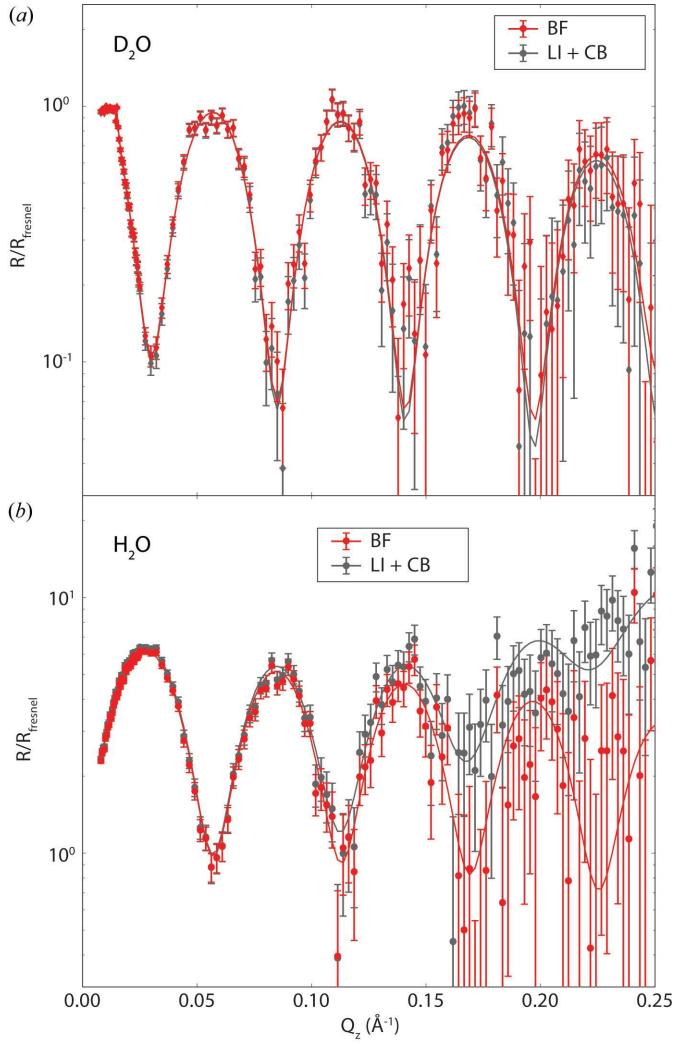

Figure 6
NR of a 100 Å thick thermal silicon oxide layer on a silicon wafer in contact with a D_2O-filled (*a*) or H_2O-filled (*b*) reservoir. Shown are data using both LI (gray) and BF (red) subtraction strategies. Solid colored lines are optimizations to a slab model. For the LI-subtracted data, a CB correction is included; for the BF-subtracted data, no CB correction is required. Reflectivities are normalized to the Fresnel reflectivity from the silicon–liquid interface. Error bars represent 68% confidence intervals based on Poisson counting statistics.

electronic reprint

Table 4
Modeling results applied to data using LI versus BF background-subtraction methods, with and without a CB correction.

Values in parentheses represent 68% confidence intervals and are approximately normally distributed (except for the D_2O SLD, which is constrained to be less than 6.4×10^{-6} Å^{-2}). nLL is the negative log-likelihood of the optimal parameters.

Method	LI	LI + CB	BF	BF + CB
D_2O				
Oxide thickness (Å)	111.67 (26)	111.62 (24)	111.66 (26)	111.66 (25)
Oxide SLD (10^{-6} Å^{-2})	3.677 (12)	3.678 (13)	3.656 (12)	3.655 (12)
D_2O SLD (10^{-6} Å^{-2})	6.3980 (17)	6.3980 (18)	6.3976 (20)	6.3976 (20)
RMS roughness (Å)	2.57 (26)	1.94 (44)	2.43 (26)	2.25 (40)
Intensity	0.9675 (27)	0.9670 (27)	0.9686 (27)	0.9684 (27)
Background (10^{-6})	—	−0.144 (72)	—	−0.037 (65)
nLL	−84.46	−82.64	−80.17	−80.06
Reduced χ^2	1.362 (47)	1.344 (57)	1.293 (47)	1.302 (57)
H_2O				
Oxide thickness (Å)	112.23 (32)	111.91 (33)	111.66 (32)	111.63 (31)
Oxide SLD (10^{-6} Å^{-2})	3.777 (37)	3.806 (37)	3.771 (39)	3.774 (38)
H_2O SLD (10^{-6} Å^{-2})	−0.179 (71)	−0.148 (82)	−0.172 (81)	−0.183 (82)
RMS roughness (Å)	1.15 (14)	3.52 (40)	2.95 (32)	3.29 (41)
Intensity	0.938 (28)	0.935 (27)	0.953 (33)	0.949 (32)
Background (10^{-6})	—	1.82 (17)	—	0.20 (17)
nLL	−122.32	−68.16	−70.63	−69.76
Reduced χ^2	1.973 (47)	1.108 (57)	1.139 (47)	1.134 (57)
Simultaneous fit				
Oxide thickness (Å)	111.84 (19)	111.78 (20)	111.69 (19)	111.68 (19)
Oxide SLD (10^{-6} Å^{-2})	3.692 (11)	3.696 (11)	3.676 (11)	3.675 (11)
D_2O SLD (10^{-6} Å^{-2})	6.3983 (16)	6.3983 (15)	6.3982 (16)	6.3981 (17)
H_2O SLD (10^{-6} Å^{-2})	−0.280 (30)	−0.267 (32)	−0.317 (30)	−0.321 (31)
RMS roughness (Å)	1.71 (27)	2.81 (29)	2.74 (19)	2.84 (27)
Intensity	0.9681 (26)	0.9698 (26)	0.9710 (26)	0.9709 (26)
D_2O background (10^{-6})	—	−0.026 (63)	—	0.042 (59)
H_2O background (10^{-6})	—	1.53 (16)	—	0.00 (15)
nLL	−222.16	−163.59	−159.93	−159.69
Reduced χ^2	1.763 (28)	1.309 (37)	1.269 (28)	1.278 (37)

statistics at each point. In principle, for monochromatic reflectometers, up to 2/3 of counting time could be spent measuring background, though in practice this is rarely the case (*e.g.* Fig. 2 shows background data that are sparse relative to the specular data). By contrast, BF subtraction incorporates all the measured background-field information in the calculated background field at any given point. As a result, BF subtraction introduces less uncertainty than LI subtraction. Indeed, if ε_{Si} is fixed, only the single free parameter εD is required to describe the entire background field.

The improvement in uncertainty introduced by background subtraction using the BF method is quantified in Fig. 7, which shows the ratio of the uncertainties introduced by LI subtraction and BF subtraction. Note that this is not the ratio of final uncertainties, as the counting uncertainty of the point at the specular ridge dominates. For LI subtraction, the uncertainty is associated with $I^{LI}_{bkg}(Q_z)$ [equation (8)]; for BF subtraction, the uncertainty is calculated by propagating the statistical uncertainty in εD through equations (16) and (24). At $Q_z = 0.25$ Å^{-1}, BF subtraction outperforms LI subtraction by a factor of 2, corresponding to a factor of 4 in counting time. Therefore, in principle, BF subtraction allows collection of

Table 5
Background-field fitting is robust against background data type or method.

Method/data used	$\varepsilon_{D_2O}D$	$\varepsilon_{H_2O}D$
Global optimization (Table 3)	0.2354 (43) × 10^{-2}	5.417 (73) × 10^{-2}
Transverse scans (Fig. 4)	0.2668 (32) × 10^{-2}	5.350 (54) × 10^{-2}
$I^+(Q_z)$ and $I^-(Q_z)$ (Fig. 2)	0.2727 (73) × 10^{-2}	5.358 (82) × 10^{-2}
Half of $I^+(Q_z)$ data	0.275 (14) × 10^{-2}	5.55 (14) × 10^{-2}
Half of $I^-(Q_z)$ data	0.273 (15) × 10^{-2}	5.35 (25) × 10^{-2}

significantly fewer background points than LI subtraction, thus improving the measurement speed.

5.4. Method robustness

To demonstrate that the BF subtraction method is robust at shorter counting times and using a variety of types of background data [in this case the transverse detector scans in Fig. 4, and $I^+(Q_z)$ and $I^-(Q_z)$ from Fig. 2], we used the *reductus* implementation to compare the background-field fits using different subsets of the background information available. The results are shown in Table 5.

Note that the values of $\varepsilon_{D_2O}D$ are slightly larger than that determined using the global optimization to the transverse detector scans reported in Table 3. The *reductus* implementation does not include the dark-count correction and the scattering parameter compensates for its absence. The much larger value of $\varepsilon_{H_2O}D$ is unaffected by this small effect.

Importantly, the background-field parameterization does not depend on which type of background data is chosen for analysis, for either H_2O or D_2O. Transverse scans and detector rotations perform equally well, as do data points on either side of the specular ridge [$I^+(Q_z)$ versus $I^-(Q_z)$]. Reducing the counting statistics increases the error bars (comparing the third and fourth rows, a factor of 2 increase in uncertainty for a factor of 4 reduction in background data used) but does not systematically affect the background-field parameterization.

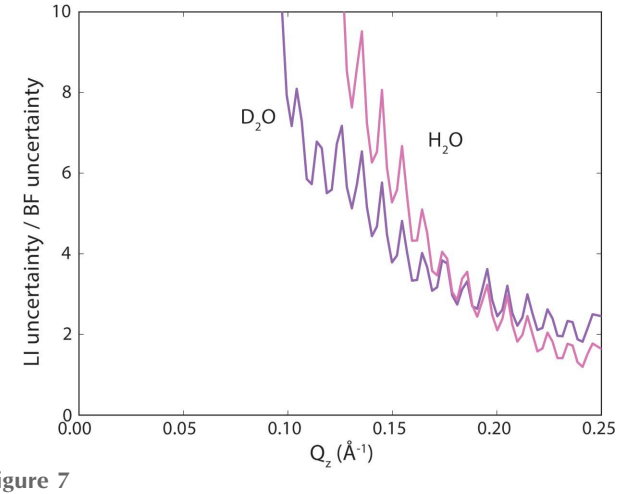

Figure 7
Ratio of uncertainties introduced by the LI and BF subtraction techniques. This ratio represents the square root of the ratio of counting times.

electronic reprint

5.5. Extension to position-sensitive detection and time-of-flight measurements

Position-sensitive (pixelated) neutron detectors are widely used on neutron reflectometers. With such detectors the data-collection rate can in principle be increased by observing the background field simultaneously with the specular reflection. The background-field method can be directly applied to this measurement scheme. Each pixel (or group of pixels in the regions of interest) is treated as an independent detector with the appropriate α_f and solid angle, which is now defined by the pixel size. The background field can then be described exactly as for a single detector. This approach involves opening the post-sample collimation to observe the background field, but simultaneously allowing each detector pixel to observe more of the beam path, particularly through air around the sample cell. Care must be taken that doing so does not introduce additional background flux to the detector and thereby degrade the signal-to-noise ratio of the measurement. To optimize the signal-to-background ratio of such a measurement, tight post-sample collimation or appropriate radial collimation is desirable.

Time-of-flight wavelength discrimination allows a broad range of wavelengths to be reflected from the sample simultaneously, enhancing data-collection rates. For the purposes of the background-field description, the time-of-flight measurement can be viewed as a parallel measurement from a series of independent monochromatic reflectometers operating with different neutron wavelengths. The background-field description [equations (16) and (24)] is thus directly applicable to each wavelength observed. In addition, if the attenuation coefficient does not have a strong dependence on neutron wavelength, *e.g.* for isotropic incoherent scattering, the background field from all wavelengths can be described using the same parameters.

6. Implications for reflectometry cell design

It is intuitive that reducing the reservoir thickness will decrease the background radiation from reservoir incoherent scattering. In Fig. 8, we explore the improvement in measured background that can be achieved by reducing the reservoir thickness. (Background subtraction further reduces the background level by about an order of magnitude.) The solid lines correspond to the predicted background level of a reflectometry cell design in which the reservoir is surrounded by thick (semi-infinite) single-crystal silicon. This design is shown in the upper left and is also used for the experiments in this article [Fig. 1(*b*)]. In this case, the path length of the neutrons through silicon, L_s, is described by equation (20). The calculation is performed for the instrument state corresponding to constant $Q_z = 0.25$ Å^{-1} using the sum of equations (16) and (24), and equation (20) for L_s. The I_{other} term is not included, as this is expected to be facility specific. The background level corresponding to a nominal 100 µm thick reservoir filled with D_2O is shown by the intersection of the vertical and horizontal dashed lines.

We estimate that to double the Q_z range, such that $Q_z^{max} = 0.5$ Å^{-1}, we require a background reduction of about a factor of 5, which is shown as the horizontal dotted line. Notably, for D_2O-based solutions, this cannot be achieved with a cell design employing thick silicon (reducing the footprint of the beam on the sample reduces the signal in proportion to the background and is not a solution).

Instead, we propose an alternative cell design employing thin silicon to enclose the reservoir, shown at the upper right of Fig. 8. In this case, the incident beam passes through the back surface of the silicon cell, rather than through the side as in the thin silicon case. For a silicon thickness t, the path length in equation (24) is $L_s = 2t/\sin\alpha_i$. With only this replacement, the colored dashed lines in the graph show the predicted background level corresponding to this cell geometry for t = 1 mm. The contribution from silicon is dramatically reduced such that the background is reduced nearly proportionately to the reservoir thickness, as predicted by equation (17). For D_2O-based solutions, a modest reduction of the reservoir thickness to 20 µm is nearly sufficient to achieve a factor of 5 reduction in background level.

For H_2O-based solutions, the scattering remains dominated by the reservoir rather than the silicon, so the benefits of reducing the silicon thickness are minimal. Thick H_2O-filled reservoirs (>180 µm, faded lines in Fig. 8) are subject to multiple scattering corrections that are not included here, so background reductions from reducing the reservoir thickness

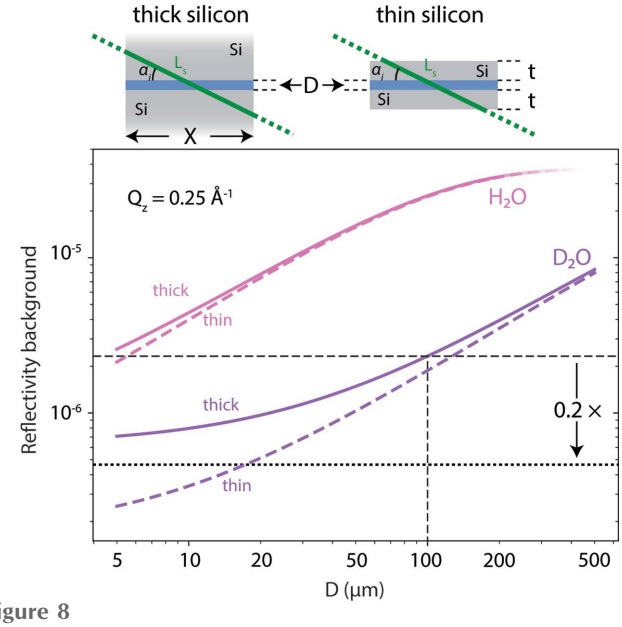

Figure 8
Effect of reflectometry cell design on the reflectivity background prior to background subtraction. (Top) Two reflectometry cell designs employing (left) thick silicon, such that the beam enters and exits the cell through the sides of the silicon, and (right) thin silicon, such that the beam enters and exits through the face of the silicon cell. (Bottom) Calculated reflectivity background for the cell designs using thick (solid lines) and thin (dashed lines) silicon. The silicon thickness has little effect on the background scattering from H_2O-filled reservoirs, but thin silicon is required to achieve large reductions in background scattering from D_2O-filled reservoirs. H_2O predictions are faded above 180 µm because of the onset of multiple scattering.

electronic reprint

may be greater than shown in the plot. However, below about 50 μm reservoir thickness the background from H_2O-filled reservoirs decreases in proportion to the reservoir thickness. Thus, the background achievable from H_2O-based measurements is limited only by the ability to fabricate extremely small reservoirs at the scale of a macroscopic block of single-crystal silicon. In principle, this reduction could approach an order of magnitude for a 5 μm reservoir thickness if the engineering and data-analysis challenges of such a design can be overcome.

7. Summary

In summary, we have shown that because of self-shielding effects the background field arising from incoherent scattering from films of intermediate thickness is anisotropic in space. For neutron reflectivity from interfaces in contact with sufficiently thin aqueous liquid reservoirs, an analytical expression for the background field is derived. This expression can be used to improve the accuracy of estimation and subtraction of the background field at the specular condition. The background-field subtraction technique yields significant improvements in background-measurement speed. Finally, we have shown that the scattering background decreases in proportion to the reservoir thickness, provided the thickness of surrounding cell materials is minimized.

Acknowledgements

We wish to thank Drs John Barker, Jeremy Cook, John Copley, Joe Dura, Peter Gehring and Paul Kienzle for helpful discussions. Samples were fabricated by Matthew Robinson at the NIST Center for Nanoscale Systems nanofabrication facility. We acknowledge the National Institute of Standards and Technology, US Department of Commerce, for providing the neutron research facilities used in this work. Certain commercial materials, equipment and instruments are identified in this work to describe the experimental procedure as completely as possible. In no case does such an identification imply a recommendation or endorsement by NIST, nor does it imply that the materials, equipment or instruments identified are necessarily the best available for the purpose.

Funding information

This work used the Extreme Science and Engineering Discovery Environment (XSEDE), which is supported by the National Science Foundation (NSF) grant No. ACI-1053575. Specifically, it used the Bridges system, which is supported by NSF award No. ACI-1445606, at the Pittsburgh Supercomputing Center. FH acknowledges support from the US Department of Commerce (grants 70NANB13H009 and 70NANB17H299).

References

Ankner, J. F., Heller, W. T., Herwig, K. W., Meilleur, F. & Myles, D. A. A. (2013). *Curr. Protoc. Protein Sci.* **72**, 17.16.1–17.16.34.
Ankner, J. F. & Majkrzak, C. F. (1992). *Proc. SPIE*, **1738**, 260–269.
Barker, J. G. & Mildner, D. F. R. (2015). *J. Appl. Cryst.* **48**, 1055–1071.
Berk, N. F. & Majkrzak, C. F. (2003). *Langmuir*, **19**, 7811–7817.
Chandrasekhar, S. (1960). *Radiative Transfer.* New York: Dover Publications.
Clifton, L. A., Ciesielski, F., Skoda, M. W. A., Paracini, N., Holt, S. A. & Lakey, J. H. (2016). *Langmuir*, **32**, 3485–3494.
Dura, J. A., Pierce, D. J., Majkrzak, C. F., Maliszewskyj, N. C., McGillivray, D. J., Lösche, M., O'Donovan, K. V., Mihailescu, M., Perez-Salas, U., Worcester, D. L. & White, S. H. (2006). *Rev. Sci. Instrum.* **77**, 074301.
Heinrich, F. & Lösche, M. (2014). *Biochim. Biophys. Acta*, **1838**, 2341–2349.
Hoogerheide, D. P., Noskov, S. Y., Jacobs, D., Bergdoll, L., Silin, V., Worcester, D. L., Abramson, J., Nanda, H., Rostovtseva, T. K. & Bezrukov, S. M. (2017). *Proc. Natl Acad. Sci. USA*, **114**, E3622–E3631.
Hottel, H. C. & Sarofim, A. F. (1967). *Radiative Transfer.* New York: McGraw-Hill.
Junghans, A., Watkins, E. B., Barker, R. D., Singh, S., Waltman, M. J., Smith, H. L., Pocivavsek, L. & Majewski, J. (2015). *Biointerphases*, **10**, 019014.
Kienzle, P. A., Krycka, J., Patel, N., Metting, C., Sahin, I., Fu, Z., Chen, W., Mont, A. & Tighe, D. (2016). *Refl1D*. Version 0.7.7. University of Maryland, College Park, MD, USA, http://reflectometry.org/danse.
Krueger, S. (2001). *Curr. Opin. Colloid Interface Sci.* **6**, 111–117.
Krueger, S., Meuse, C. W., Majkrzak, C. F., Dura, J. A., Berk, N. F., Tarek, M. & Plant, A. L. (2001). *Langmuir*, **17**, 511–521.
Majkrzak, C. F., Berk, N. F., Krueger, S. & Perez-Salas, U. A. (2006). *Neutron Scattering in Biology: Techniques and Applications*, edited by J. Fitter, T. Gutberlet & J. Katsaras, pp. 225–263. Berlin, Heidelberg: Springer-Verlag.
Majkrzak, C. F., Berk, N. F. & Perez-Salas, U. A. (2003). *Langmuir*, **19**, 7796–7810.
Maranville, B., Ratcliff, W. II & Kienzle, P. (2018). *J. Appl. Cryst.* **51**, 1500–1506.
Nylander, T., Campbell, R. A., Vandoolaeghe, P., Cardenas, M., Linse, P. & Rennie, A. R. (2008). *Biointerphases*, **3**, FB64–FB82.
Nystrom, N. A., Levine, M. J., Roskies, R. Z. & Scott, J. R. (2015). *Proceedings of the 2015 XSEDE Conference: Scientific Advancements Enabled by Enhanced Cyberinfrastructure*, Article 30. New York: ACM.
Schalke, M. & Lösche, M. (2000). *Adv. Colloid Interface Sci.* **88**, 243–274.
Sears, V. F. (1992). *Neutron News*, **3**(3), 26–37.
Towns, J., Cockerill, T., Dahan, M., Foster, I., Gaither, K., Grimshaw, A., Hazlewood, V., Lathrop, S., Lifka, D., Peterson, G. D., Roskies, R., Scott, J. R. & Wilkins-Diehr, N. (2014). *Comput. Sci. Eng.* **16**, 62–74.
Vrugt, J. A., ter Braak, C. J. F., Diks, C. G. H., Robinson, B. A., Hyman, J. M. & Higdon, D. (2009). *Int. J. Nonlin. Sci. Num. Simul.* **10**, 273–290.

electronic reprint